

Localized Surface Plasmon Enhanced Laser Reduction of Graphene Oxide for Wearable Strain Sensor

Author

Wan, Z, Wang, S, Haylock, B, Wu, Z, Nguyen, TK, Phan, HP, Sang, R, Nguyen, NT, Thiel, D, Koulakov, S, Trinchì, A, Gao, Y, Lobino, M, Li, Q

Published

2021

Journal Title

Advanced Materials Technologies

Version

Accepted Manuscript (AM)

DOI

[10.1002/admt.202001191](https://doi.org/10.1002/admt.202001191)

Rights statement

© 2021 WILEY-VCH Verlag GmbH & Co. KGaA, Weinheim. This is the peer reviewed version of the following article: Localized Surface Plasmon Enhanced Laser Reduction of Graphene Oxide for Wearable Strain Sensor, Advanced Materials Technologies, 2021, which has been published in final form at <https://doi.org/10.1002/admt.202001191>. This article may be used for non-commercial purposes in accordance with Wiley Terms and Conditions for Self-Archiving (<http://olabout.wiley.com/WileyCDA/Section/id-828039.html>)

Downloaded from

<http://hdl.handle.net/10072/403733>

Griffith Research Online

<https://research-repository.griffith.edu.au>

Localized Surface Plasmon Enhanced Laser Reduction of Graphene Oxide for Wearable Strain Sensor

Zhengfen Wan ^{a, b}, Shujun Wang ^{a, b}, Ben Haylock ^c, Zhiqing Wu ^{a, b}, Khoa-Nguyen Tuan ^a,
Hoang-Phuong Phan ^a, Robert Sang ^c, Nam-Trung Nguyen ^a, David Thiel ^b, Sergio Koulakov ^d,
Adrian Trinchì ^e, Yongsheng Gao ^{b, f}, Mirko Lobino ^{a, c}, Qin Li ^{a, b, *}

^a *Queensland Micro- and Nanotechnology Centre, Griffith University, Nathan, QLD 4111, Australia*

^b *School of Engineering and Built Environment, Griffith University, Nathan, QLD 4111, Australia*

^c *Centre for Quantum Dynamics, School of Environment and Science, Griffith University, Nathan, QLD 4111 Australia*

^d *Aquarius Technologies Pty Ltd., 19 Overlord Place, Acacia Ridge, QLD 4110, Australia*

^e *CSIRO Manufacturing, Clayton, VIC 3168, Australia*

^f *Institute for Integrated Intelligent Systems, Griffith University, Nathan, QLD 4111, Australia*

^{*} *Corresponding author: Prof. Qin Li, Tel: +61 7 3735 7514, qin.li@griffith.edu.au*

Abstract

Laser reduced graphene has been increasingly attracting broad attention owing to its unique properties and potential applications in energy conversion and storage, flexible electronics, optoelectronics and nanocomposites. In this study, we fabricated graphene sheets decorated with Au nanoparticles *in situ* using milliwatt femtosecond laser reduction. Our findings revealed an enhancement in both the reduction of graphene oxide sheets and the nucleation and growth of the Au nanoparticles during the *in-situ* laser treatment. We consider the three stages of reactions, namely, (i) the spontaneous redox reaction between HAuCl₄ and graphene oxide, (ii) the laser-induced decomposition of HAuCl₄ and reduction of graphene oxide and, (iii) the localized surface plasmon resonance enhanced photoreduction in the presence of Au particles. The resulting

graphene/Au nanoparticle composite possesses charge mobility ($946 \text{ cm}^2 \text{ V}^{-1} \text{ s}^{-1}$), 10-fold that of pure laser reduced graphene ($94 \text{ cm}^2 \text{ V}^{-1} \text{ s}^{-1}$). Moreover, the Au nanoparticles formed densely and evenly distributed square-lattice-like microcrack networks that ensured a linear resistance change over the tested strain range. This microcrack network architecture enables the development of flexible graphene/Au strain sensors with gauge factors up to 52.5, linear behaviour up to 25% strain and excellent repeatability (over 500 cycles). This strain sensor was also demonstrated to monitor human motions. Our findings leveraged the resistive properties of graphene/metal nanoparticle composites with fundamental physical chemistry, electronic properties and mechanical mechanisms, laying a critical step towards highly functional, low-cost, flexible and wearable graphene-based electronics.

Keywords: Laser reduced graphene oxide, localized surface plasmon resonance, surface plasmon enhanced reduction, strain sensor, flexible device

Introduction

Surface plasmon (SP), a collective electron oscillation along the surface of a metal, typically observed in gold (Au) or silver (Ag), has been studied extensively for various advanced applications [1] such as, surface plasmon resonance sensors [2] and surface enhanced Raman scattering (SERS) [3]. Within a lifetime of 10 fs [4], the surface plasmon decays by photon emission or by exciting energetic charge carriers, which rapidly thermalize with the metal lattice at a time scale of a few picoseconds [5]. In the thermal decay, the metal nanoparticles can serve as photothermal sources and perform as local nanoantennae to enhance the optical energy absorption at a selected plasmon frequency [6]. Ratchford reported that before the thermalization of these hot carriers, the loss of surface plasmons can induce charge transfer from the metal to the adjacent semiconductors, generating a current or driving a chemical reaction [7]. This plasmon-induced charge transfer process can be employed to improve photocatalysis, fabricate photodetectors, or stimulate selective photochemistry.

Graphene has drawn tremendous attention due to its extraordinary properties including high electrical and thermal conductivities, optical transparency, and high mechanical strength [8-10]. Among diverse fabrication methods of graphene [11, 12], laser reduced graphene oxide (LRGO) has recently attracted significant interest [13-16], owing to its suitability for industrial production, and localized treatment and patterning without the use of chemicals [17-19]. Based on the LRGO,

various applications have been demonstrated such as supercapacitors, sensors, field effect transistors, solar cells and optical devices [20, 21]. Due to the facile fabrication and accessible measurement of electrical signal, resistive sensors have become one of the most studied sensors. [22] However, the quality of LRGO varies greatly, depending on the laser wavelength, pulse frequency and power. Femtosecond laser induced LRGO has the advantage of refined spatial resolution and low laser power demand, albeit the resultant LRGO graphenenity and conductivity are typically low [19].

Flexible strain sensors utilizing graphene are receiving increased attention for their tremendous potential in health monitoring, artificial skins, robotic sensors, and human-machine interfaces [23, 24]. Tian et al. reported a graphene strain sensor with a gauge factor (GF) of 9.49 (strain up to 10%) by directly reducing GO film with a light-scribe DVD burner [25]. Carvalho et al. demonstrated a low-cost laser-induced graphene strain sensor with a GF of 40 and strain only up to 1.5% by ultraviolet irradiation of commercial polyimide [26]. Besides the pure graphene, Ren and coworkers reduced GO films doped with Ag nanoparticles with a 450 nm laser, which resulted in a LRGO/Ag strain sensor exhibiting nonlinear relationship between strain and the relative resistance change (GF of 183 within strain 0%–8%, GF of 475 within strain 8%–14.5%) [26]. This nonlinearity, which makes the calibration process complex and difficult, is considered as one of the major drawbacks of resistive type strain sensors [27]. Thus, further investigation into the laser reduction method is imperative to develop the flexible strain sensor with wide detection range, high sensitivity and a more linear behaviour. The crack in the graphene strain sensor was considered to be the main mechanism to induce the resistance change [25]. We hypothesize that the key factor for a graphene-based strain sensor to offer good linearity over a large strain range relies on the control of the cracks in the graphene film, where the cracks function as the displacement-determined resistors. Dense and evenly distributed cracks in high quality graphene films will significantly improve the performance of strain sensors.

Herewith, we introduce a new class of LRGO/Au strain sensors by simultaneously reducing GO film mixed with HAuCl_4 solution with a femtosecond (fs) laser. Our strain sensor shows high sensitivity (GF 52.5), excellent stretchability (strain up to 25.4%), full-range linear behaviour and excellent stability (500 testing cycles and consistent operation over 1 year). Furthermore, we investigated the underlying mechanisms of the improved strain sensing performance of the LRGO/Au composites formed by laser treatment. The localized surface plasmon resonance (LSPR) of the Au nanoparticles enhanced the reduction of GO. Moreover, the emergence of Au nanoparticles between graphene sheets enhances the generation and propagation of film microcracks by serving as the strain concentration spots. Both the enhanced reduction of GO and the increased microcracks contribute to the excellent performance of the LRGO/Au strain sensor.

Results and Discussion

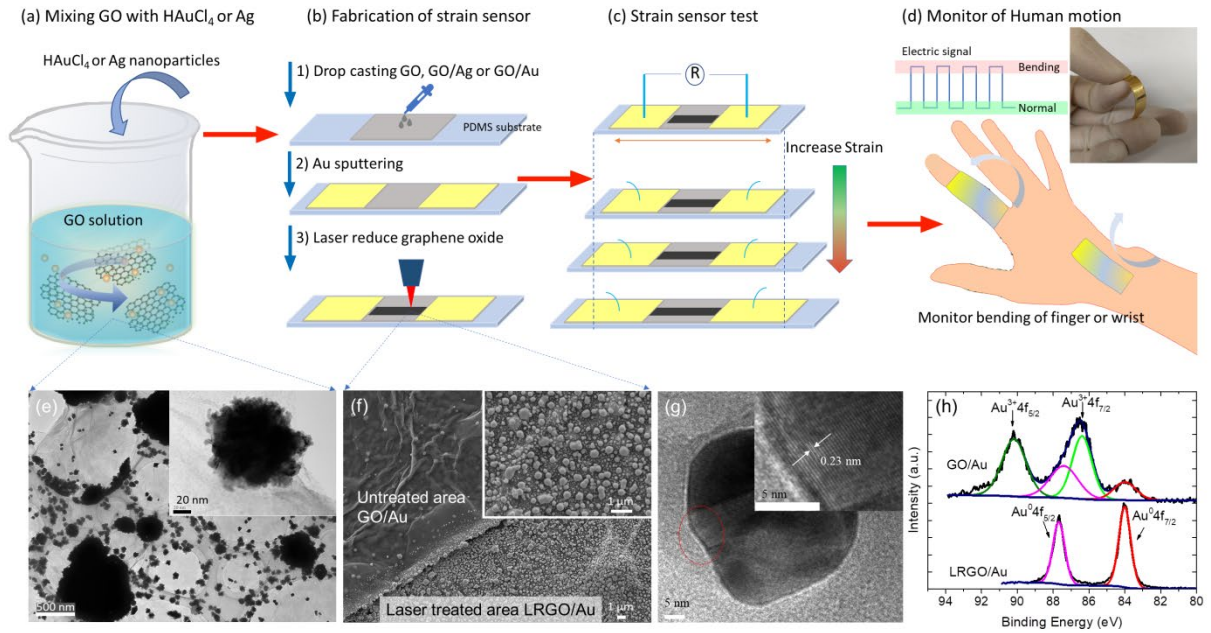


Figure 1 The schematic of the mixing of GO with HAuCl₄ or Ag nanoparticles (a), the fabrication process of the sensor (b), the test of strain sensor (c), and the application of monitoring human motion (d). The inset of image (d) shows the photograph of the strain sensor. (e) The TEM image of GO/Au, the inset is the enlarged image. The scale bar is 500 nm and its inset is 20 nm. (f) The SEM images of GO/Au partly treated by laser with the bird's eye view. The scale bar is 1 μm. Its inset is the overall SEM image of laser treated area with scale bar of 1 μm. (g) The TEM image of LRGO/Au and its zoom-in image, the scale bar is 5 nm. (h) The comparison of Au4f XPS spectra of GO/Au and LRGO/Au (power 5 mW, scan speed 5 μm/s).

Figure 1(a) schematically illustrates the mixing of GO solution with HAuCl₄ or Ag nanoparticles (NPs). The fabrication process of the sensor is shown in Figure 1(b) and the detailed description presented in the experimental section. To test the sensor, the resistance is measured subject to variations in strain, as in Figure 1(c). We demonstrated practical applications of the as-fabricated strain sensors in monitoring human motions and gestures by attaching the sensor onto the finger or wrist, Figure 1(d).

Figure 1(e) shows the TEM image of GO/HAuCl₄ mixture when drop cast onto the PDMS substrate. The size of the NPs on the GO sheets ranges from tens of nanometers up to around 1 μm . The inset shows the magnified image of a small NP of about 50 nm. An EDX analysis (Figure S1(a)) of these NPs reveals the amount of elemental Au is much greater than chlorine (atomic concentration 98% Au, 2% Cl), indicating that a part of AuCl₄⁻ was reduced to Au and these NPs are a mixture of HAuCl₄ precipitates and Au. The aromatic conjugated domains are hypothesized to act as electron-donating sources to reduce Au³⁺ to Au nanoparticles after the mixture of HAuCl₄ and GO [28]. Therefore, redox reactions between GO and HAuCl₄ can spontaneously take place without external stimuli, which is consistent with our observation.

SEM images of the untreated and laser-treated GO/HAuCl₄ composite film, Figure 1(f), show an obvious step between the laser treated area and the untreated area. This step is likely caused by laser burning, thermally removing a part of the GO sheets from the top surface [29]. Figure 1(f) clearly shows that before laser treatment, the Au NPs were sparsely distributed on the GO top layer, whilst after the laser treatment, the density of the Au NPs has been tremendously increased accompanied with a morphology change. The inset image reveals that the size of the nano Au particles on the top surface after the laser treatment varied from tens to about 400 nm, suggesting some NPs have merged into larger sizes.

HRTEM image of Au NP on LRGO/Au film, Figure 1(g), shows that the rough surface edges of NPs in the GO/Au mixture, Figure 1(e), have become smooth after the laser treatment, indicating the undergoing of thermal annealing. The measured lattice spacing is 0.23 nm, close to the lattice spacing (0.236 nm) corresponding to the spacing of the (111) crystal plane of face-centered cubic gold [30]. Figure 1(h) illustrates the peak fitted Au 4f XPS spectra of GO/Au and LRGO/Au (5 mW). The Au⁰4f_{5/2} (87.4 eV) and Au⁰4f_{7/2} (84 eV) peaks represent the binding energies of reduced Au particles, while Au³⁺4f_{5/2} (90.2 eV) and Au³⁺4f_{7/2} (86.4 eV) peaks correspond to the binding energies of Au ions [31, 32]. For the mixture of GO/HAuCl₄, both the peaks of Au⁰ and Au³⁺ are observable, confirming the existence of both reduced Au particles and Au ions. For LRGO/Au, only the peak of Au⁰ can be observed. It can be concluded that all the Au ions on the surface were reduced to Au⁰ particles with laser treatment, and the initial spontaneous reduction of Au³⁺ only converted a fraction of the Au³⁺ in the mixture.

Laser reduction of GO/Au

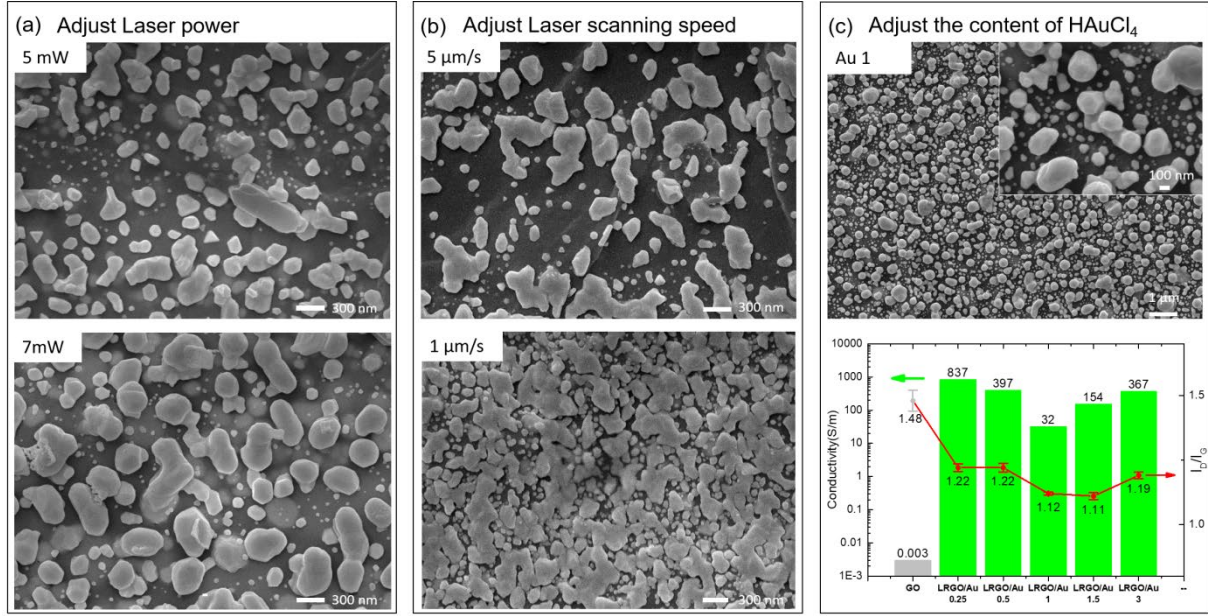


Figure 2 The SEM images, I_D/I_G in Raman and conductivity of LRGO/Au with different Au contents. (a) The SEM images of the LRGO/Au with average laser power of 5 mW and 7 mW at a scan speed of 20 μm/s. The scale bar is 300 nm. (b) The SEM images of the LRGO/Au with average laser power of 3 mW at a scan speed of 5 μm/s and 1 μm/s. The scale bar is 300 nm. (c) The SEM images of the LRGO/Au 1 and the I_D/I_G in Raman spectra and conductivity of LRGO/Au with different Au content of 0.25, 0.5, 1, 1.5 and 3. The scale bar of SEM image is 1 μm and its inset is 100 nm.

The surface morphology of LRGO/Au can be modulated by adjusting the laser power and scanning speed of the femtosecond laser. Figure S2(a-b) shows the SEM image of LRGO/Au as a function of the laser power and scanning speed. Increasing the laser power from 5 mW to 7 mW, the sparsely distributed Au nanoparticles on the top surface of LRGO/Au turn to be denser and larger in size, as shown in Figure 2(a). From Figure 2(b) it is clear that decreasing the laser scanning speed from 5 μm/s down to 1 μm/s also enhances the density of Au nanoparticles. Figure 2(c) and Figure S2(c) demonstrate the SEM image of LRGO/Au under various quantity ratios (0.25, 0.5, 1, 1.5, 3) as well as their I_D/I_G of Raman spectra and conductivity. The LRGO/Au 0.25 and LRGO/Au 0.5 show the partial removal of the surface, exposing some Au nanoparticles. For LRGO/Au 1 and LRGO/Au 1.5, the GO on the top surface was completely burned away and numerous Au nanoparticles emerged. The significant structural modifications can be reflected in their Raman spectra of GO and LRGO/Au (0.25, 0.5, 1, 1.5, 3). For LRGO/Au (0.25, 0.5, 1, 1.5, 3), the band intensity ratio (I_D/I_G) which indicates the degree of disorder in the graphene-structure decreases greatly compared to that of GO. The conductivity of LRGO/Au is enhanced to 837 S/m (for LRGO/Au 0.25), 5 orders of magnitude larger than that of GO. For the Au concentrations studied,

the conductivity of LRGO/Au varies from 32 to 837 S/m. This improved conductivity well agrees with fewer observed structural defects in the Raman spectra.

Figure 3 shows the peak fitted C1s XPS spectra of GO, GO/Au, LRGO and LRGO/Au. The spectra of GO and GO/Au in Figure 3(a-b) show an increase in C-O bond after mixing GO with HAuCl₄, suggesting the Redox reaction between GO and HAuCl₄, where GO is oxidized. The XPS results of LRGO treated at the laser power of 3 and 5 mW (scan speed 5 μ m/s) in Figure S3(a) and Figure 3(c) reveal that only a small amount of oxygen content (about 5%) was removed. In contrast, the same laser treatment (3 or 5 mW with scan speed 5 μ m/s) on GO/Au resulted in significantly improved oxygen removal as shown by the C1s high resolution scan in Figure S3(b) and Figure 3(d). Table S1 in Supporting Information lists the atomic concentration percentage of all chemical states of GO, GO/Au, LRGO and LRGO/Au in the XPS spectra. The CC refers to the sum of C-C sp² and C-C sp³ and the CO is the combination of C-O, C=O and COOH. Figure 3(e) shows that the percentage ratio of the CC bond to the CO bond (CC/CO) rises from 0.80 (GO/Au) to 2.85 (LRGO/Au 5 mW), which is more than two-fold increase than the system containing only GO, 1.19 (LRGO 5 mW). This data illustrates the superior of the LRGO/Au binary system in removing oxygen under mW femtosecond laser treatment.

It can be concluded that after the incorporation of Au nanoparticles, the reduction of GO is significantly improved, which may result from the LSPR of Au nanoparticles. The LSPR of Au or Ag nanoparticles derives from the photo-induced collective oscillation of conduction band electrons [33], which can participate in the reaction or produce heat by self-collision [34]. It was reported that, as highly active photocatalysts, the hot electrons excited by the LSPR of noble nanoparticles are injected into the conduction band of GO, resulting its reduction [35]. Also, most of the hot electrons transfer their energy to heat by electron-electron or electron-phonon collisions [33]. The resulting photothermal effect contribute to the enhanced reduction of GO. The surface plasmon absorption of Au nanoparticles can be tuned over a broad range, from 517 to 575 nm by adjusting size [36], and from 600 to 873 nm by changing the particle geometry [37]. Since the wavelength of our laser is 780 nm and the Au nanoparticles are irregularly shaped, as seen in Figure 2(c), the enhanced oxygen removal can be ascribed to the LSPR of the reduced Au nanoparticles. Moreover, the intense thermal effect induced by the LSPR can also melt Au nanoparticles, resulting in the merging of small nanoparticles into larger sizes.

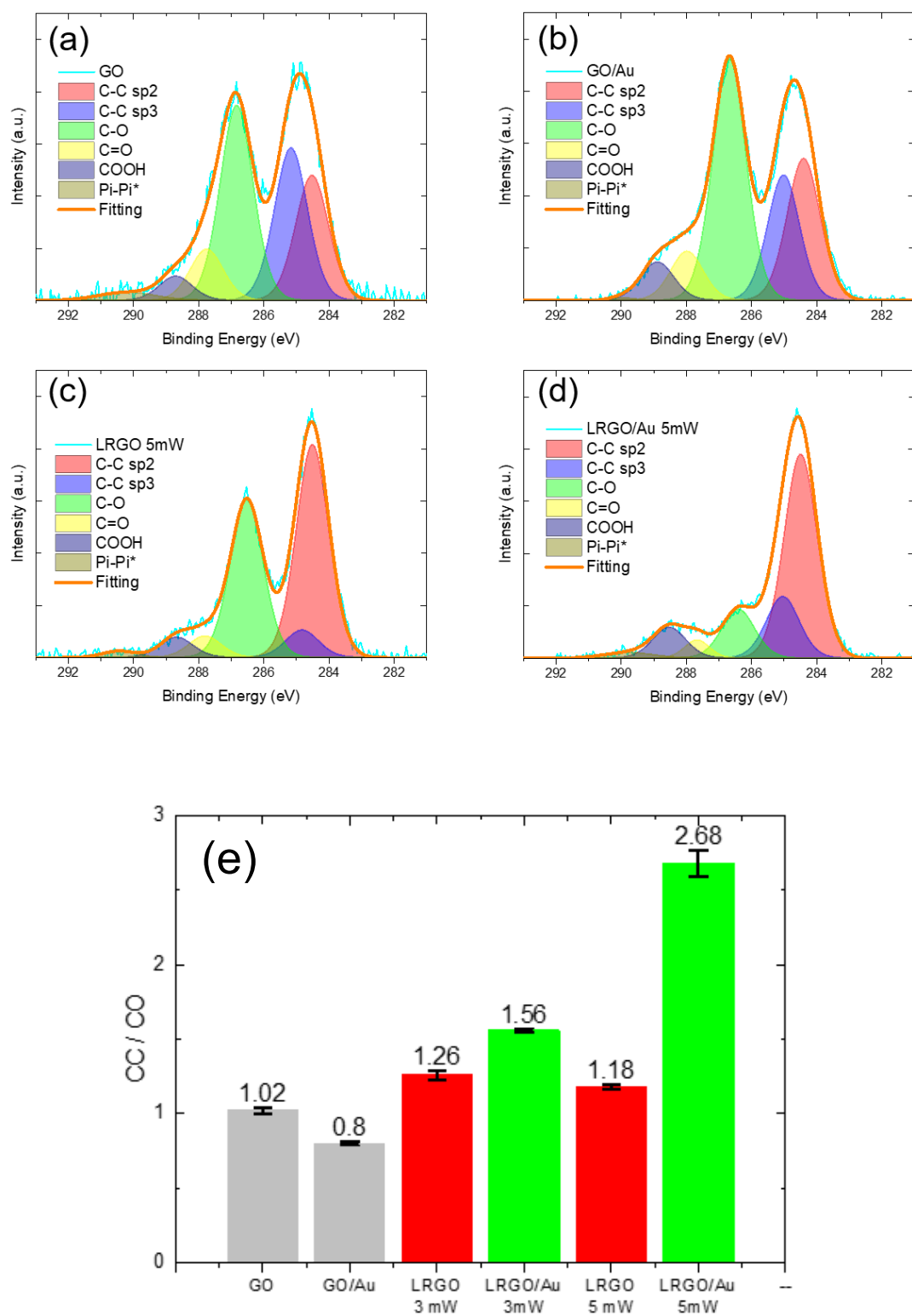
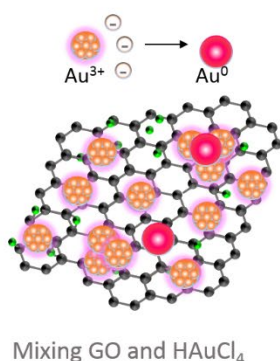


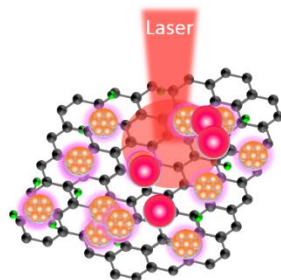
Figure 3 (a-f) Peak fitted C1s XPS spectra of GO (a), GO/Au (b), LRGO treated with 5 mW laser (c), LRGO/Au treated with 5 mW laser (d). (e) The ratio of the percentage of CC bond to that of CO bond with different samples.

Figure 4 summarizes the reactions in the LRGO/Au formation process. When GO was mixed with HAuCl₄ in solution, a redox reaction occurred where HAuCl₄ was partially reduced to Au nanoparticles and GO was oxidized, as shown by the XPS data in Figure 1(h) and 3(b). The reduction potential of AuCl₄⁻¹ (0.76V vs. SCE, saturated calomel electrode) is higher than that of GO (0.48 V vs. SCE) [38, 39]. During laser reduction on the film of GO intercalated with the mixture of HAuCl₄ precipitates and Au NPs, the decomposition of HAuCl₄ to Au and the partial reduction of GO occurs simultaneously by the photoreduction of the laser. Zhao *et al.* proposed that the HAuCl₄ was reduced to Au nanoparticles due to the multiphoton process of the 800 nm femtosecond laser [40]. Thermal decomposition of HAuCl₄ to Au occurs at a temperature above 160 °C [41]. Meanwhile, the reduction of GO results from both the photochemical and photothermal effects of laser [20, 42]. Therefore, the decomposition of HAuCl₄ and the reduction of GO are attributed to both laser induced photothermal and photochemical effects. Unique to the binary composite film of GO/ HAuCl₄ as the population of Au NPs increased under the laser treatment, the laser reduction effect on GO magnified owing to the LSPR effect. The LSPR has been reported to enhance the photothermal efficiency [43, 44] as well as to induce charge transfer for the photochemical reaction [45]; both mechanisms could be at play, contributing to the significantly enhanced photothermal and photochemical effects in the laser reduction process for reducing HAuCl₄ to Au NPs and GO to LRGO. These photo-reduced Au nanoparticles will continually boost the entire reduction process, which eventually results in the highly reduced GO and dense Au nanoparticles on the surface. Figure S3(c) illustrates the XPS of GO/Au and LRGO/Au treated with 5 mW laser at different scan speeds. The LRGO/Au demonstrates a high degree of oxygen removal at scan speeds of 5 μm/s, 10 μm/s and 20 μm/s. After mixing with Au nanoparticles, the high reduction efficiency of GO can be achieved with an increasing laser scan speed.

1. The redox reaction between GO and AuCl_4^{-1}



2. The decomposition of HAuCl_4 and the reduction of GO



3. The LSPR enhanced photoreduction

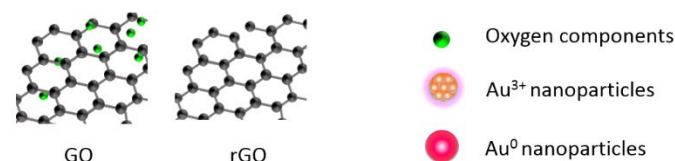
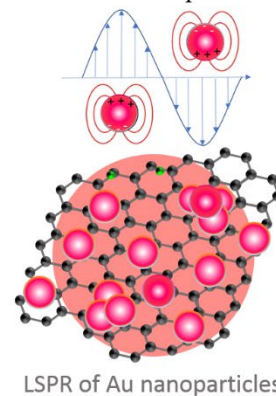


Figure 4 The schematic illustration of reactions of GO/Au in the whole process

To verify the role of LSPR in laser induced GO reduction, Ag NPs of 30-nm diameter were also mixed with GO for laser treatment, as shown by the TEM image in Figure S4(a). Figure S4(b-d) shows the SEM image of the Ag-doped GO sample. Figure S4(b) shows the SEM image of partially reduced GO/Ag at a low magnification. A notable contrast in morphology between the laser treated area and untreated area is observed. Figure S4(c) shows a magnified SEM image of GO/Ag, where aggregation of Ag nanoparticles into several hundreds of nanometers among the GO is seen. The magnified SEM image of LRGO/Ag Figure S4(d) illustrates the partly sunken surface of the film, which may result from the exposure of air trapped inside the GO/Ag during film fabrication after a part of the GO material on the surface was burned away by the laser. Figure S4(e) shows the EDX of particles of LRGO/Ag, verifying the content of silver in the film.

The XPS comparison of GO/Ag and post-treatment LRGO/Ag (power 5 mW, scanning speed 5 $\mu\text{m/s}$), Figure 5(a-b), also showed significantly enhanced removal of C-O bonds, similar to that of LRGO/Au. The localized plasmon resonance frequency of Ag nanoparticles can also be tuned to cover a broad range by varying their sizes and shapes, for instance, from 400 to 700 nm in one study [46]. The pre-formed Ag NPs appeared to concentrate more photothermal energy, since our SEM investigation observed uniformly distributed ‘holes’ a few micrometer apart on the LRGO/Ag film, which is an indication of locally intensified thermal ablation. The XPS analysis suggests that the LSPR effect of Ag NPs has enhanced the removal of C-O bond, similar to LRGO/Au.

From the Raman spectra of GO (a), LRGO (5mW) (b), LRGO/Au (5mW) (c), LRGO/Ag

(5mW) (d) shown in Figure S5, the band intensity ratio (I_D/I_G) is extracted as the indicator for the degree of graphitization, displayed in Figure 5(c). After being treated with laser (5 mW), the I_D/I_G of LRGO (1.35) only slightly decreased compared to that of the parent material, GO (1.37). The introduction of metal NPs has induced a considerable decrease of I_D/I_G , namely 1.17 for LRGO/Au and 1.22 for LRGO/Ag, suggesting a larger average size of the sp^2 domains of LRGO/Au and LRGO/Ag than that of LRGO [47].

Figure 5(d) shows the carrier mobility of GO, LRGO, LRGO/Au and LRGO/Ag (all subjected to 5 mW power and at 5 $\mu\text{m/s}$ scanning speed) obtained from the Hall effect measurement. The carrier mobility of LRGO reaches $94\text{ cm}^2\text{ V}^{-1}\text{ s}^{-1}$, much larger than that of GO ($11\text{ cm}^2\text{ V}^{-1}\text{ s}^{-1}$), due to fewer defects/impurities and larger graphitic sp^2 domains after laser reduction [48]. It's worth noting that the carrier mobility of LRGO/Au was further improved to $946\text{ cm}^2\text{ V}^{-1}\text{ s}^{-1}$, attributed to the enhanced reduction of GO and the effective bridging of Au nanoparticles between reduced GO sheets. On the other hand, the LRGO/Ag exhibits a lower carrier mobility of $10\text{ cm}^2\text{ V}^{-1}\text{ s}^{-1}$, which may result from Ag nanoparticles induced gaps between LRGO sheets and the incongruent contacts between Ag nanoparticles and LRGO sheets. The different result of LRGO/Ag and LRGO/Au might be caused by the better matching between the LSPR frequency of Au nanoparticles with the laser, than that of Ag nanoparticles. Evidently, metal nanoparticles can be applied for the improvement of laser reduction of GO and the LSPR is a reasonable mechanism behind the enhanced reduction.

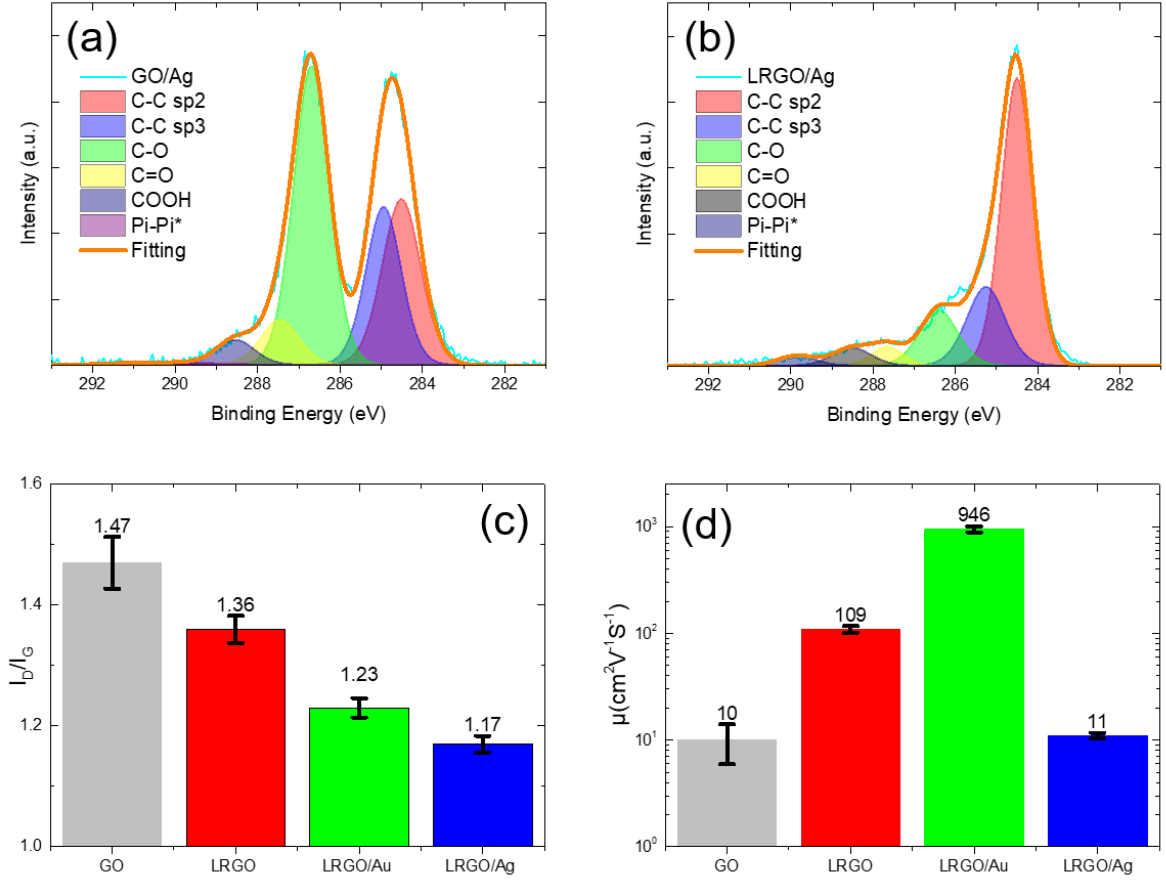


Figure 5 (a-b) The XPS spectra of GO/Ag and LRGO/Ag (5 mW). (c) The I_D/I_G of GO, LRGO, LRGO/Au and LRGO/Ag treated with 5 mW laser. (d) The carrier mobility of GO, LRGO, LRGO/Au and LRGO/Ag treated with 5 mW laser.

Strain sensor application

The electrical resistance of LRGO, LRGO/Ag and LRGO/Au on the flexible substrate (i.e. PDMS) was measured under applied strains and the gauge factors (GF) were calculated.

$$GF = (\Delta R/R_0)/\varepsilon$$

where, the ΔR is the resistance change; R_0 the initial resistance; ε the strain.

Figure 6(a) and (b) present the I-V curves and the relative resistance change ($\Delta R/R_0$) of the LRGO under different strains measured with the two-probe configuration, respectively. It is clear that LRGO is almost insensitive to strain, with an extremely small GF of about 0.1 over a wide strain range up to 21%. For the LRGO sensor, the resistance between neighboring graphene sheets is determined by their overlapping areas and the contact resistances, while the sliding of graphene sheets is the dominant mechanism resulting in resistance change under strain [25]. Figure 6(c) shows the response of the LRGO/Au sensor under varied strains. The current of LRGO/Au

decreased markedly with the increase in strain, which is directly resulted from the increase in the resistance of LRGO/Au. Figure 6(d) plots the relative resistance change of LRGO/Au under strains ranging from 0% to 25.4%, corresponding to a large GF of 52.5 throughout the strain range of 0%–25.4%, which is extraordinary for a flexible strain sensor. The strain sensing performance of LRGO/Ag shows higher sensitivity, however, with two linear regimes, namely GF=64 in strain range of 0%–15.3%, and GF=133 in the range of 15.3%–24.7%, Figure 6(e-f).

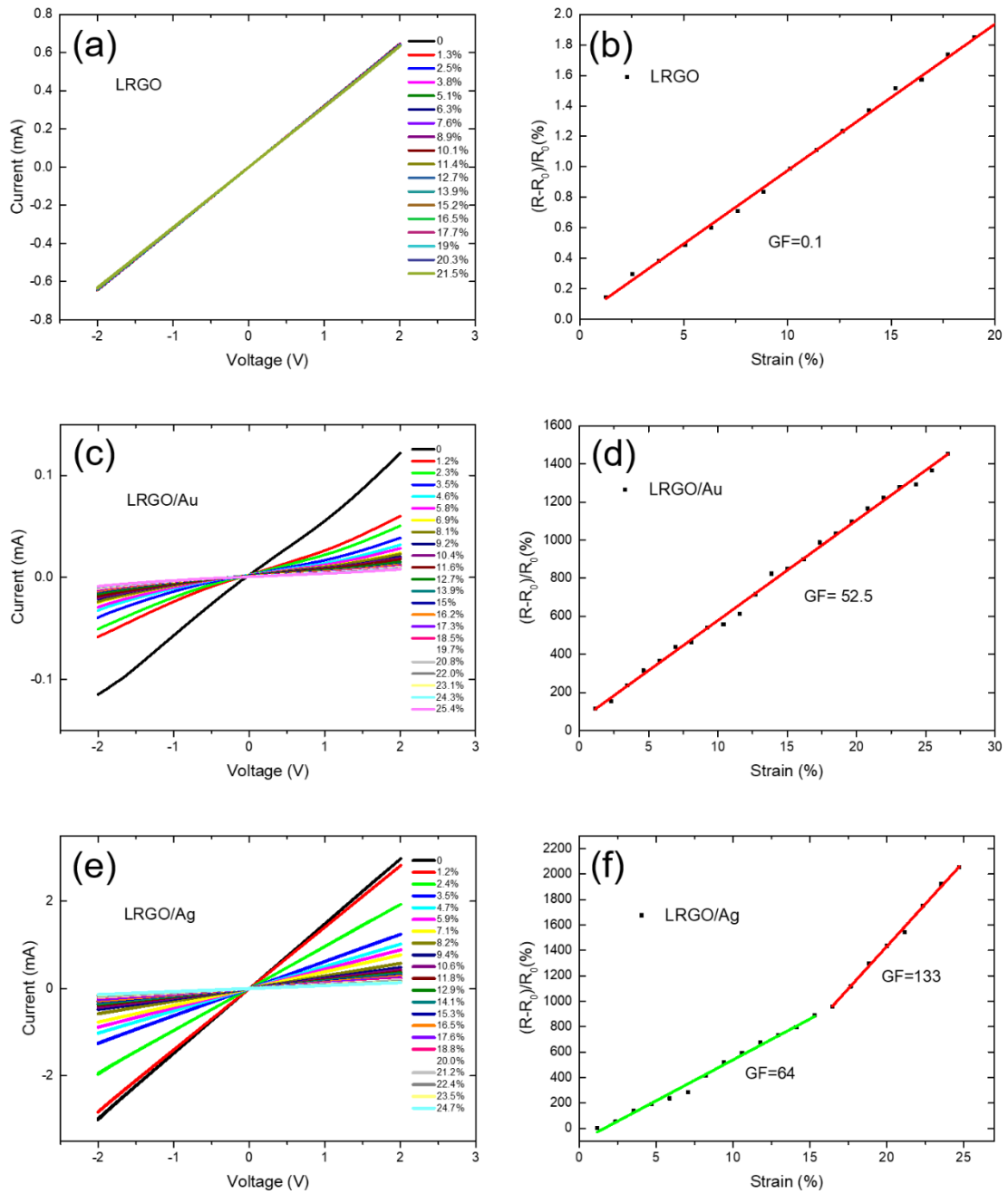


Figure 6 (a,c,e) The I-V curves under different strain of LRGO (a), LRGO/Au (c) and LRGO/Ag (e). (b,d,f)

The relative resistance change under different strains: (b) LRGO, The GF was 0.1 under 21% strain. (f) LRGO/Au, the GF was 52.5 under 25.4% strain. (d) LRGO/Ag, the GF was 64 under 15.3% strain, 133 under 24.7% strain.

Figure 7(a-c) shows the microscopic images of LRGO, LRGO/Au and LRGO/Ag under strains of 5%, 10% and 20%. It can be noted that as the strain increased from 5% to 20%, all the three samples demonstrate expanded cracks, which extended the conducting paths and increase the electrical resistance under mechanical elongation. For the strain above 25.4%, the LRGO/Au film peels off the PDMS substrate. Figure 7(a) illustrates the cracks of LRGO, which are mostly formed in the transverse direction with respect to the stretching force. Figure 7(b-c) illustrates that the density of the cracks on LRGO/Au is much higher in comparison to LRGO. In addition, the cracks of LRGO/Au developed in both transverse and longitudinal directions, forming a lattice of cracks. An examination of the LRGO/Ag film shows the fractures were developed in somewhat random fashion. The modified cracks in the LRGO/metal NPs systems is likely due to the localized intense thermal effect that was induced by LSPR of metal NPs. The metal NPs thermally etch the adjacent GO sheets and create numerous pores, which could function as the initiating points for the formation of cracks [33]. The magnified microscopic images of LRGO, LRGO/Au and LRGO/Ag in Figure S6 illustrate the development of cracks under strain.

Figure 7(b) shows the schematic conductive path of LRGO/Au with cracks under an applied strain of 10%. The emerged microcracks on the film reshape the conductive path and affect the resistance [49]. The different cracking behaviours between LRGO/Au and LRGO/Ag may be due to the fact that the Au NPs were formed and merge into the LRGO sheets in the laser reduction process, while the Ag nanoparticles were synthesized *a priori*. The distribution of Au nanoparticles in the composite film is much more uniform than that of Ag NPs in LRGO sheets. Therefore, the cracks in LRGO/Au film are in a regular lattice format. When the film is stretched in uniaxial direction, the cracks perpendicular to the stretching direction expanded, while those in the parallel direction mostly closed off gradually. The denser the cracks are, the smaller the displacement is under the same stress. If this widening of the cracks occurs in a more evenly distributed manner, then the chance of break-off of the weakest link is reduced, and this is the primary reason for the emergence of multiple GF ranges. The closing-off of some of the cracks in the direction parallel to the stretching may reduce the resistance change, but likely has a positive effect on maintaining a reasonable conductivity under large strain. Compared to the expansion of cracks of LRGO and LRGO/Au, the cracks of the LRGO/Ag do not only expand with the increased strain but also break into isolated islands, which could completely alter the conductive path and result in its nonlinear behavior as strain sensor. When the strain is lower than 15.3%, GF = 64, and the GF reaches 133

within the strain range of 15.3%–24.7%. This sensing performance is attributed to the structure change of the conductive network within the LRGO/Ag strain sensor. Under the strain below 15.3%, microcracks were developed between stacked LRGO flakes, contributing to the $GF = 64$. Since the Ag nanoparticles were simply mixed with the GO flakes, which is different from the *in-situ* fabricated Au nanoparticles, the connections between Ag nanoparticles and LRGO flakes are unconsolidated. When a large external strain of more than 15.3% is applied, parts of the contacts between Ag nanoparticles and LRGO flakes were separated, restricting the charge transport. These disconnections result in a large increase in resistance and the big $GF = 133$ of the strain sensor.

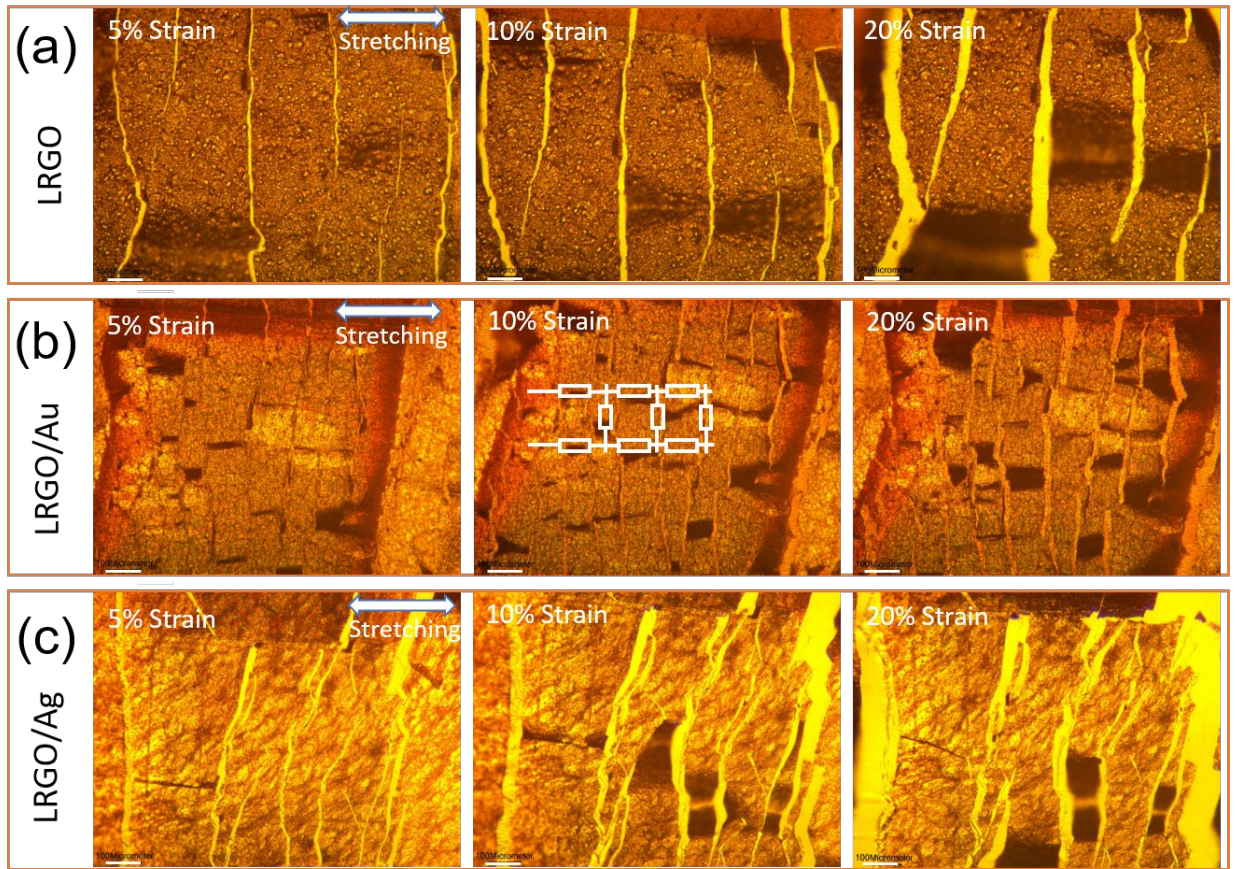


Figure 7 (a-c) The microscopic images of LRGO(a), LRGO/Au (b), LRGO/Ag (c) under different applied strains: 5% (left), 10% (middle) and 20% (right). The scale bar is 100 μm . The Schematic conductive path of LRGO/Au under the strain of 10% was shown in Figure (b) (middle).

Due to its excellent flexibility and sensitivity, the LRGO/Au possesses significant potential for application in wearable sensors for monitoring human activities, as demonstrated by the videos in Supporting Information. Here, we assembled a LRGO/Au sensor to monitor the wrist and finger movements with the relative resistance change, where R_0 is the initial resistance and R is the real-

time resistance. Figure 8(a) shows a real-time response of the sensor with the movement of the wrist. Figure 8(b) shows the response of the sensor while moving the finger to press a computer mouse button. Clear relative resistance change can be observed when the wrist or finger performs different gestures. After more than 500 cycles, the LRGO/Au strain sensor still demonstrated excellent stability and repeatability, Figure 8(c-d). The stretchability and high sensitivity in the LRGO/Au demonstrate its promise for ubiquitous wearable sensing applications.

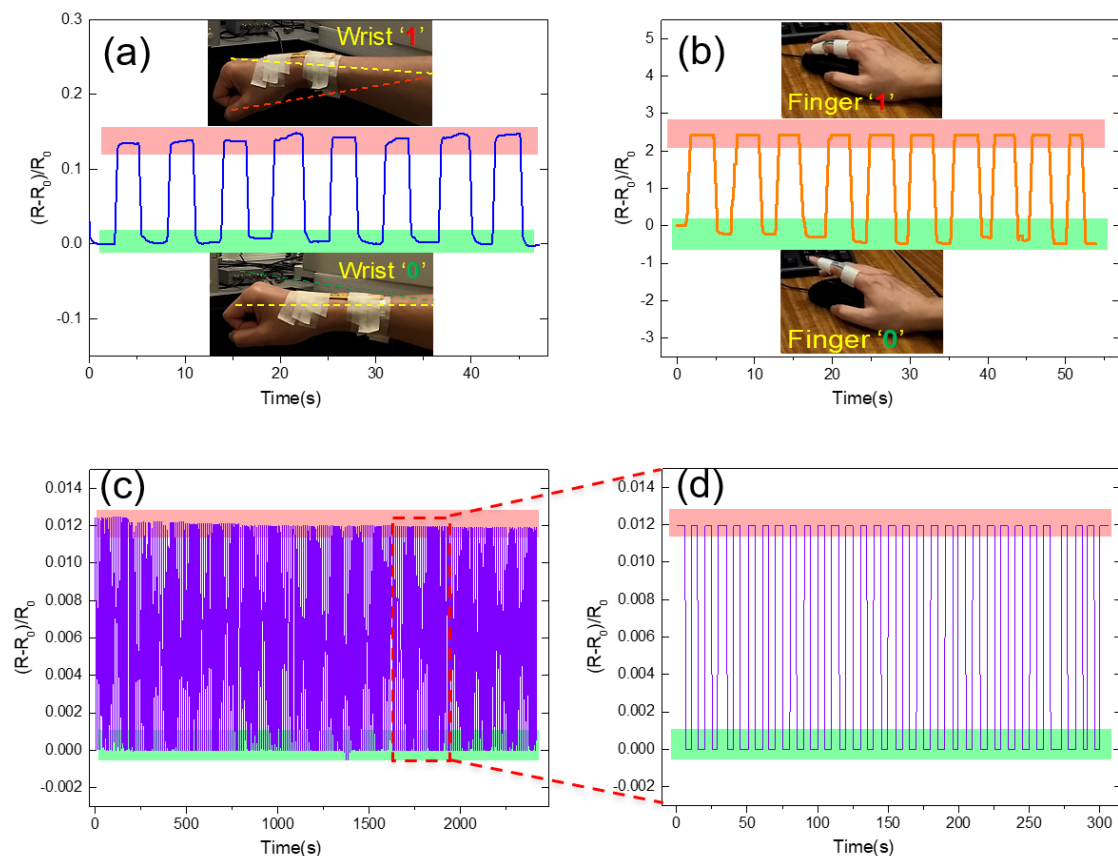


Figure 8 (a-b) Detection of human motions. The sensor assembled on the wrist (a) and finger (b). (c-d) Relative resistance change at cycling test, demonstrating excellent stability.

Other related publications for wearable strain sensor were listed in **Table 1**. Compared to other reports, the simple laser direct writing method shows great advantage of facile and flexible manufacture. The fabricated LRGO/Au strain sensor shows a good linearity with GF 64 within the strain range of 25.4%. It demonstrates great potential for integrated wearable devices in motion monitor and health management.

Table 1. Performance comparison of wearable strain sensor”

Material	Performance	Reference
Au nanowire	GF 6.9 in the strain range of 0%–5%; GF 9.9 for the strain < 50%; Maximum strain range 350 %	[50]
Au nanowire	Maximum GF 1365; Maximum strain range 80%	[51]
Graphene	GF about 1 with strain of 15%	[52]
LRGO	GF 9.49 in strain range of 10 %	[25]
LRGO/Au	GF 52.5 in strain range of 25.4%	this work
LRGO/Ag	GF 4 in strain range of 0%–15.3%; GF 133 in strain range of 15.3%–24.7%	this work

Conclusions

We presented a facile, one-step laser treatment on the composites of HAuCl_4 and GO to fabricate wearable LRGO/Au strain sensor, which shows a high GF of 52.5 and excellent linearity in a large strain range up to 25.4%, as well as good stability within 500 tested cycles. Importantly, we found that under low power near-infrared (NIR) laser treatment (780 nm femtosecond), the LSPR of the reduced Au nanoparticles further enhances the reduction of GO, producing higher grapheninity, likely due to a combination of photothermal and surface plasmon-induced charge transfer. Our results demonstrated that the LSPR of both Au or Ag can unequivocally enhance the reduction degree of GO with a standard laser system. The enhancement in the reduction of GO and *in-situ* formation and insertion of these noble metal nanoparticles markedly increased the carrier mobility by an order of magnitude ($946 \text{ cm}^2 \text{ V}^{-1} \text{ s}^{-1}$) in comparison to the LRGO alone ($94 \text{ cm}^2 \text{ V}^{-1} \text{ s}^{-1}$). Moreover, the introduction of Au or Ag nanoparticles between graphene sheets increases the generation and propagation of film microcracks. Both the augmented electrical properties and the increased mechanical microcracks under strain contribute to the improved performance of LRGO/Au strain sensor. The LRGO/Au strain sensors were demonstrated to detect various human motions such as folding and unfolding of wrist and finger, highlighting their significant potential for use in artificial skin and wearable electronics.

Experiment

Method

GO was prepared using the modified Hummers method [53, 54]. The GO was dispersed in water with a concentration of 2.4 g/L. For the mixture of HAuCl_4 and GO, 420 mg HAuCl_4 was added into the 10 ml of GO solution (2.4 g/L). The solution was mixed with magnetic stir for 30 minutes and the solution container was covered with alumina foil, avoiding light. The mixture of HAuCl_4 and GO is termed as GO/Au. The laser treated mixture of HAuCl_4 and GO is termed as LRGO/Au. The GO mixed with various weight of HAuCl_4 were treated with laser and denoted as LRGO/Au X (X=0.25, 0.5, 1, 1.5 or 3), where X signifies the times of the weight of the HAuCl_4 precursor in the GO solution to that in the aforementioned GO/Au solution. Silver nanoparticles were synthesized with AgNO_3 and polyvinylpyrrolidone [55]. The size of the Ag particles is about 30 nm. The Ag colloidal dispersion with a silver concentration of 1g/L was mixed with the aforementioned GO solution with ultrasound (ratio 1:1). The mixture of Ag nanoparticles and GO is termed as GO/Ag. Polydimethylsiloxane (PDMS) SYLGARD 184 silicone elastomer was purchased from Dow Corning GmbH for the fabrication of substrate. The PDMS substrate was cleaned by isopropanol and pure water with ultrasound. After cleaning, the PDMS was dried at 60 °C for 1 hour and then treated with air plasma for 1 minute before usage.

The GO, GO/Ag, or GO/Au dispersion was drop-casted on the PDMS substrate. After being dried at 60°C for 1 hour, the GO, GO/Ag, or GO/Au films were fabricated. For the fabrication of strain sensors, after the fabrication of GO, GO/Ag, or GO/Au film, gold electrodes with a thickness of about 150 nm were deposited on the films with a sputter. The gap between the electrodes is around 1,000 μm . Then a laser treatment was conducted in between the gaps under ambient conditions. A 780 nm fs pulse laser (70 fs pulse width, 50 MHz repetition rate and spot size of 2 μm diameter), was employed for reduction under ambient conditions. A silver paste (resin #186-3616 from RS Components) was used to connect the electrodes of samples with electric wires for electrical test.

Characterization

The scanning electron microscopy (SEM) images were obtained using JEOL JSM-7001F, equipped with the energy-dispersive X-ray spectroscopy (EDX) system. The transmission electron microscopy (TEM) images were acquired with TECNAI F20 equipped with EDX system. The

optical micrographs were obtained with a microscope from ProSciTech, camera UCMOS05100KPA. Raman spectra were acquired with Raman Spectrometer Renishaw Invia (using 514 nm excitation wavelength and a 50× objective, acquisition parameters: 0.05 mW power, 10 s exposure time, 3 accumulations, and 2400 l/m gridding). Peak fittings of the Raman data were carried out using the WiRE3.3 software. The x-ray photoelectron spectroscopy (XPS) measurement was performed with Kratos Axis ULTRA X-ray Photoelectron Spectrometer (with a monochromated Al Ka radiation). The peak fitting of the XPS data was carried out using the CasaXPS software.

The PDMS substrate with the LRGO device was mounted on a micrometre caliper, which induced strain by controlling the length of the PDMS substrate. Electrical properties were measured with a Model 6430 source meter (Keithley Instruments Inc.) and a B1505A Power Device Analyzer (Agilent Technologies Inc.).

Acknowledgements

Z. Wan thanks to the support of the Griffith University International Postgraduate Scholarship and a CSIRO Top-up Scholarship. The authors acknowledge the funding support of Australian Research Council (ARC) Industry Transformational Research Hub (IH 180100002) and ARC Discovery Project (DP200101105). This work was performed in part at the Queensland node of the Australian National Fabrication Facility, a company established under the National Collaborative Research Infrastructure Strategy to provide nano- and micro-fabrication facilities for Australia's researchers. M. Lobino was supported by the ARC Future Fellowship (FT180100055). The authors also thank the technical support from the Queensland Micro- and Nanotechnology Centre at Griffith University, and the Centre for Microscopy and Microanalysis at the University of Queensland.

References

- [1] M. Sun, Nanoparticle Catalysis by Surface Plasmon, in: S.L. Suib (Ed.), *New and Future Developments in Catalysis*, Elsevier, Amsterdam, 2013, pp. 473-487.
- [2] H. Liao, C.L. Nehl, J.H. Hafner, Biomedical applications of plasmon resonant metal nanoparticles, *Nanomedicine (Lond)* 1(2) (2006) 201-8.
- [3] J. Langer, D. Jimenez de Aberasturi, J. Aizpurua, et al., Present and Future of Surface-Enhanced Raman Scattering, *ACS Nano* 14(1) (2020) 28-117.
- [4] S. Link, M.A. El-Sayed, Shape and size dependence of radiative, non-radiative and photothermal properties of gold nanocrystals, *Int. Rev. Phys. Chem.* 19(3) (2000) 409-453.
- [5] G.V. Hartland, Optical studies of dynamics in noble metal nanostructures, *Chem. Rev.* 111(6) (2011) 3858-87.
- [6] R. Hushka, J. Zuloaga, M.W. Knight, et al., Light-induced release of DNA from gold nanoparticles: nanoshells and nanorods, *J. Am. Chem. Soc.* 133(31) (2011) 12247-55.
- [7] D.C. Ratchford, Plasmon-Induced Charge Transfer: Challenges and Outlook, *ACS Nano* 13(12) (2019) 13610-13614.
- [8] Y. Huang, J. Liang, Y. Chen, An overview of the applications of graphene-based materials in supercapacitors, *Small* 8(12) (2012) 1805-34.
- [9] Y. Liu, X. Dong, P. Chen, Biological and chemical sensors based on graphene materials, *Chem. Soc. Rev.* 41(6) (2012) 2283-307.
- [10] A.K. Geim, K.S. Novoselov, The rise of graphene, *Nat. Mater.* 6(3) (2007) 183-91.
- [11] R. Ye, D.K. James, J.M. Tour, Laser-Induced Graphene: From Discovery to Translation, *Adv. Mater.* 31(1) (2019) e1803621.
- [12] R. Ye, J.M. Tour, Graphene at Fifteen, *ACS Nano* 13(10) (2019) 10872-10878.
- [13] L. Huang, Y. Liu, L.-C. Ji, et al., Pulsed laser assisted reduction of graphene oxide, *Carbon* 49(7) (2011) 2431-2436.
- [14] K.H. Ibrahim, M. Irannejad, M. Hajialamdari, et al., A Novel Femtosecond Laser-Assisted Method for the Synthesis of Reduced Graphene Oxide Gels and Thin Films with Tunable Properties, *Adv. Mater. Interfaces* 3(14) (2016) 1500864.
- [15] Y. Zhao, Q. Han, Z. Cheng, et al., Integrated graphene systems by laser irradiation for advanced devices, *Nano Today* 12 (2017) 14-30.
- [16] R. Arul, R.N. Oosterbeek, J. Robertson, et al., The mechanism of direct laser writing of graphene features into graphene oxide films involves photoreduction and thermally assisted structural rearrangement, *Carbon* 99 (2016) 423-431.
- [17] N.-Q. Deng, H. Tian, Z.-Y. Ju, et al., Tunable graphene oxide reduction and graphene patterning at room temperature on arbitrary substrates, *Carbon* 109 (2016) 173-181.
- [18] Y.C. Guan, Y.W. Fang, G.C. Lim, et al., Fabrication of Laser-reduced Graphene Oxide in Liquid Nitrogen Environment, *Sci. Rep.* 6 (2016) 28913.
- [19] Z. Wan, S. Wang, B. Haylock, et al., Tuning the sub-processes in laser reduction of graphene oxide by adjusting the power and scanning speed of laser, *Carbon* 141 (2019) 83-91.
- [20] Z. Wan, E.W. Streed, M. Lobino, et al., Laser-Reduced Graphene: Synthesis, Properties, and Applications, *Adv. Mater. Technol.* 3(4) (2018) 1700315.
- [21] N. Kurra, Q. Jiang, P. Nayak, et al., Laser-derived graphene: A three-dimensional printed

- graphene electrode and its emerging applications, *Nano Today* 24 (2019) 81-102.
- [22] N.N. Jason, M.D. Ho, W. Cheng, Resistive electronic skin, *J. Mater. Chem. C* 5(24) (2017) 5845-5866.
- [23] H.P. Phan, Y. Zhong, T.K. Nguyen, et al., Long-Lived, Transferred Crystalline Silicon Carbide Nanomembranes for Implantable Flexible Electronics, *ACS Nano* 13(10) (2019) 11572-11581.
- [24] T. Nguyen, T. Dinh, A.R.M. Foisal, et al., Giant piezoresistive effect by optoelectronic coupling in a heterojunction, *Nat. Commun.* 10(1) (2019) 4139.
- [25] H. Tian, Y. Shu, Y.L. Cui, et al., Scalable fabrication of high-performance and flexible graphene strain sensors, *Nanoscale* 6(2) (2014) 699-705.
- [26] Z. Yang, D.Y. Wang, Y. Pang, et al., Simultaneously Detecting Subtle and Intensive Human Motions Based on a Silver Nanoparticles Bridged Graphene Strain Sensor, *ACS Appl. Mater. Interfaces* 10(4) (2018) 3948-3954.
- [27] M. Amjadi, K.-U. Kyung, I. Park, et al., Stretchable, Skin-Mountable, and Wearable Strain Sensors and Their Potential Applications: A Review, *Adv. Funct. Mater.* 26(11) (2016) 1678-1698.
- [28] R.Z. Li, R. Peng, K.D. Kihm, et al., High-rate in-plane micro-supercapacitors scribed onto photo paper using in situ femtolaser-reduced graphene oxide/Au nanoparticle microelectrodes, *Energy Environ. Sci.* 9(4) (2016) 1458-1467.
- [29] C. Mattevi, G. Eda, S. Agnoli, et al., Evolution of Electrical, Chemical, and Structural Properties of Transparent and Conducting Chemically Derived Graphene Thin Films, *Adv. Funct. Mater.* 19(16) (2009) 2577-2583.
- [30] Y.Q. Wang, W.S. Liang, C.Y. Geng, Coalescence Behavior of Gold Nanoparticles, *Nanoscale Res. Lett.* 4(7) (2009) 684-8.
- [31] M. Sankar, Q. He, M. Morad, et al., Synthesis of stable ligand-free gold-palladium nanoparticles using a simple excess anion method, *ACS Nano* 6(8) (2012) 6600-13.
- [32] N. Zhang, H. Qiu, Y. Liu, et al., Fabrication of gold nanoparticle/graphene oxide nanocomposites and their excellent catalytic performance, *J. Mater. Chem.* 21(30) (2011) 11080-11083.
- [33] X. Wang, M. Zhu, W. Fu, et al., Au nano dumbbells catalyzed the cutting of graphene oxide sheets upon plasmon-enhanced reduction, *RSC Adv.* 6(52) (2016) 46218-46225.
- [34] X. Wang, M. Zhu, Y. Sun, et al., A New Insight of the Photothermal Effect on the Highly Efficient Visible-Light-Driven Photocatalytic Performance of Novel-Designed TiO₂ Rambutan-Like Microspheres Decorated by Au Nanorods, *Part. Part. Syst. Charact.* 33(3) (2016) 140-149.
- [35] T. Wu, S. Liu, Y. Luo, et al., Surface plasmon resonance-induced visible light photocatalytic reduction of graphene oxide: using Ag nanoparticles as a plasmonic photocatalyst, *Nanoscale* 3(5) (2011) 2142-4.
- [36] S. Link, M.A. El-Sayed, Spectral Properties and Relaxation Dynamics of Surface Plasmon Electronic Oscillations in Gold and Silver Nanodots and Nanorods, *J. Phys. Chem. B* 103(40) (1999) 8410-8426.
- [37] Yu, S.-S. Chang, C.-L. Lee, et al., Gold Nanorods: Electrochemical Synthesis and Optical Properties, *J. Phys. Chem. B* 101(34) (1997) 6661-6664.
- [38] H. Zhang, J.-J. Xu, H.-Y. Chen, Shape-Controlled Gold Nanoarchitectures: Synthesis, Superhydrophobicity, and Electrocatalytic Properties, *J. Phys. Chem. C* 112(36) (2008) 13886-

13892.

- [39] X. Chen, G. Wu, J. Chen, et al., Synthesis of "clean" and well-dispersive Pd nanoparticles with excellent electrocatalytic property on graphene oxide, *J. Am. Chem. Soc.* 133(11) (2011) 3693-5.
- [40] C. Zhao, S. Qu, J. Qiu, et al., Photoinduced formation of colloidal Au by a near-infrared femtosecond laser, *J. Mater. Res.* 18(7) (2011) 1710-1714.
- [41] S.M. Yoon, U.J. Kim, A. Benayad, et al., Thermal conversion of electronic and electrical properties of AuCl₃-doped single-walled carbon nanotubes, *ACS Nano* 5(2) (2011) 1353-9.
- [42] L. Guo, R.-Q. Shao, Y.-L. Zhang, et al., Bandgap Tailoring and Synchronous Microdevices Patterning of Graphene Oxides, *J. Phys. Chem. C* 116(5) (2012) 3594-3599.
- [43] A.F. Zedan, S. Moussa, J. Ternier, et al., Ultrasmall gold nanoparticles anchored to graphene and enhanced photothermal effects by laser irradiation of gold nanostructures in graphene oxide solutions, *ACS Nano* 7(1) (2013) 627-36.
- [44] D.K. Lim, A. Barhoumi, R.G. Wylie, et al., Enhanced photothermal effect of plasmonic nanoparticles coated with reduced graphene oxide, *Nano Lett.* 13(9) (2013) 4075-9.
- [45] S. Linic, U. Aslam, C. Boerigter, et al., Photochemical transformations on plasmonic metal nanoparticles, *Nat. Mater.* 14(6) (2015) 567-76.
- [46] J.J. Mock, M. Barbic, D.R. Smith, et al., Shape effects in plasmon resonance of individual colloidal silver nanoparticles, *J. Chem. Phys.* 116(15) (2002) 6755-6759.
- [47] F. Tuinstra, J.L. Koenig, Raman Spectrum of Graphite, *J. Chem. Phys.* 53(3) (1970) 1126-1130.
- [48] Y. Wang, Y. Chen, S.D. Lacey, et al., Reduced graphene oxide film with record-high conductivity and mobility, *Mater. Today* 21(2) (2018) 186-192.
- [49] X. Liao, Z. Zhang, Z. Kang, et al., Ultrasensitive and stretchable resistive strain sensors designed for wearable electronics, *Mater. Horiz.* 4(3) (2017) 502-510.
- [50] S. Gong, D.T.H. Lai, B. Su, et al., Highly Stretchy Black Gold E-Skin Nanopatches as Highly Sensitive Wearable Biomedical Sensors, *Adv. Electron. Mater.* 1(4) (2015) 1400063.
- [51] S. Gong, L.W. Yap, B. Zhu, et al., Local Crack-Programmed Gold Nanowire Electronic Skin Tattoos for In-Plane Multisensor Integration, *Adv. Mater.* 31(41) (2019) 1903789.
- [52] S. Kabiri Ameri, R. Ho, H. Jang, et al., Graphene Electronic Tattoo Sensors, *ACS Nano* 11(8) (2017) 7634-7641.
- [53] W.S. Hummers, R.E. Offeman, Preparation of Graphitic Oxide, *J. Am. Chem. Soc.* 80(6) (1958) 1339-1339.
- [54] W. Wang, E. Eftekhari, G. Zhu, et al., Graphene oxide membranes with tunable permeability due to embedded carbon dots, *Chem. Commun.* 50(86) (2014) 13089-13092.
- [55] K. TekaiiaáElhsissen, Preparation of colloidal silver dispersions by the polyol process. Part 1—synthesis and characterization, *J. Mater. Chem.* 6(4) (1996) 573-577.